Unraveling the Oxidation of a Graphitic Lattice: Structure Determination of Oxygen Clusters

Mohammad Tohidi Vahdat,[1,2,*] Shaoxian Li,[1,*] Shiqi Huang,[1] Carlo A. Pignedoli,[3] Nicola Marzari,[2,†] and Kumar Varoon Agrawal[1,‡]

[1]*Laboratory of Advanced Separations (LAS), École Polytechnique Fédérale de Lausanne (EPFL), CH-1950 Sion, Switzerland*
[2]*Theory and Simulation of Materials (THEOS) and National Centre for Computational Design and Discovery of Novel Materials (MARVEL), EPFL, CH-1015 Lausanne, Switzerland*
[3]*Swiss Federal Laboratories for Materials Science and Technology (EMPA), CH-8600 Dübendorf, Switzerland*

(Received 10 February 2023; accepted 14 September 2023; published 18 October 2023)

Unraveling the oxidation of graphitic lattice is of great interest for atomic-scale lattice manipulation. Herein, we build epoxy cluster, atom by atom, using Van der Waals' density-functional theory aided by Clar's aromatic π-sextet rule. We predict the formation of cyclic epoxy trimers and its linear chains propagating along the armchair direction of the lattice to minimize the system's energy. Using low-temperature scanning tunneling microscopy on oxidized graphitic lattice, we identify linear chains as bright features that have a threefold symmetry, and which exclusively run along the armchair direction of the lattice confirming the theoretical predictions.

DOI: 10.1103/PhysRevLett.131.168001

The chemical functionalization of graphitic materials (graphene, carbon nanotubes, fullerenes) has been heavily investigated to control electronic, optoelectronic, and barrier properties. Oxidation has been a method of choice given its simplicity and scalability. The oxidation of graphitic lattice has been widely studied to understand the formation of graphite and graphene oxide [1–3], to unzip carbon nanotubes [4,5], to synthesize graphene nanoribbons [6,7], and to incorporate vacancy defects in graphene [8–10]. Mechanistic understanding of the structural evolution of the graphitic lattice during the oxidation process is of fundamental interest. Such understanding will accelerate efforts to gain atomic-scale control over lattice oxidation to advance the applications in electronics [11–14], optoelectronics [12,13,15,16], optics [17], magnetism [18], and mass transport [8,19–23]. However, despite a widescale adaptation of oxidation, the underlying evolution of graphitic structure, even at the early stage of oxidation, remains debated. There is no consensus on the structure of oxidized graphitic lattice.

It is now agreed that oxidation of the graphitic lattice proceeds with the chemisorption of oxygen in the form of an epoxy group [24–29]. Epoxy group is favored as the chemisorption product because it does involve a splitting of the C—C bond of the lattice. For example, epoxy group is predicted to form from the chemisorption of O_3 on graphene with a low energy barrier of 0.72 eV [30]. The epoxy groups are highly mobile with a low energy barrier for diffusion (0.7 eV) over the lattice corresponding to a hopping timescale of seconds at room temperature [30,31]. This allows epoxy groups to form clusters minimizing the net energy of the functionalized lattice [32]. Continued oxidation leads to the formation of large clusters where lattice is strained. This considerably weakens the C—C bond close to the chemisorbed O [33]. Further energy stimulus then initiates a chain of events relieving the lattice strain by the cleavage of the C—C bond, e.g., by the formation of ether, and ultimately by gasification leading to the formation of vacancy defects [34,35].

Understanding the formation of epoxy clusters and the corresponding organization of epoxies in the cluster is crucial to control defect morphology at the atomic scale. However, the clustering of epoxy continues to be debated mainly due to the challenges in validating the cluster structure arising from the high reactivity of epoxy groups. Progress toward imaging of epoxy groups was made recently where isolated epoxies on the graphene lattice were visualized by scanning tunneling microscopy (STM) [28]. However, clusters were not observed because the O coverage in this study was low (below 0.01 monolayer).

Because of the lack of experimental data, the current understanding of epoxy clustering is from *ab initio* studies to predict and compare cluster binding energy. Li *et al.* were the first to show that two epoxy groups prefer to sit on the opposite ends of the honeycomb (henceforth referred as para-dimer configuration) [32]. In this configuration, the epoxies are separated by two C—C bridges. Later, by using a larger (7×7) graphene supercell, Sun *et al.* showed that the two epoxies in dimer prefer to be separated by a single C—C bridge (henceforth referred as meta-dimer configuration) [33].

The continued addition of epoxy has been predicted to form elongated clusters or linear chains in a bid to explain the crack formation and unzipping of graphitic materials. A frequently proposed chain structure is one formed by

 © 2023 American Physical Society

organization of epoxy chain running along the zigzag direction of the lattice where honeycomb hosts two oxygen in the para configuration [Fig. S7(b)]. However, such a configuration is doubtful when isolated dimers prefer the meta configuration.

In this Letter, we address the longstanding questions on the evolution of the epoxy cluster. Using the Van der Waals (VdW) density-functional theory (DFT), we show that the epoxy cluster indeed evolves as a linear chain; however, the chain is composed of a cooperative assembly of cyclic trimers that uniquely follow the armchair direction to minimize the net energy of the system. We validate the predicted structure by synthesizing epoxy clusters on the graphitic lattice and imaging them using low-temperature STM (LTSTM). We indeed observe the formation of linear chains that show a good agreement with the predicted structure, including chain propagation along the armchair direction. Taken together, we reveal step-by-step formation of the linear epoxy chain that opens a new direction for precise atomic-scale control for lattice functionalization and patterning.

To understand the evolution of the epoxy cluster, we built several structural models representing clusters formed by dimers, trimers, tetramers, and pentamers. The graphitic substrate was modeled using bilayer graphene (supercell made of 7×7 periodic unit cells) representing a supported graphene layer (consistent with the graphitic substrate used in the experiments as discussed later). We calculated cluster energy, defined as the net energy of the cluster in a given configuration. Next, we compared the cluster energy for isomers (defined as clusters hosting the same number of epoxies) to arrive at the most probable isomer.

For dimers, we computed the cluster energy for the most probable isomers [33] where epoxies are placed inside a single honeycomb in the para and in the meta configurations [Figs. 1(a) and 1(b), Fig. S1]. The VdW-DFT calculation indicated that the cluster energy of the meta configuration was lower than that of the para configuration by 0.73 eV, making the former favorable [Table S1]. This comparison is consistent with the comparison of the binding energy of the isomer (Supplemental Material [36], Note S1). This finding can be explained by the Clar's aromatic π-sextet rule, which has been successfully used in the past to describe the relative stability of polyaromatic hydrocarbons and graphene nanoribbons (Supplemental Material, Note S2) [31,52]. The isomer with the largest number of π sextets is more favorable because this represents a smaller disruption to the aromaticity of the lattice [52–54]. To understand this, we drew a graphene lattice hosting ten π sextets [Fig. 1(c)]. Then we drew the two dimer and counted the number of π sextets. Indeed, meta-dimer has one more π sextet than para-dimer.

Given the predictive nature of Clar's theory on the most probable cluster, we drew structural models of isomers of larger epoxy clusters (trimers, tetramers, and pentamers)

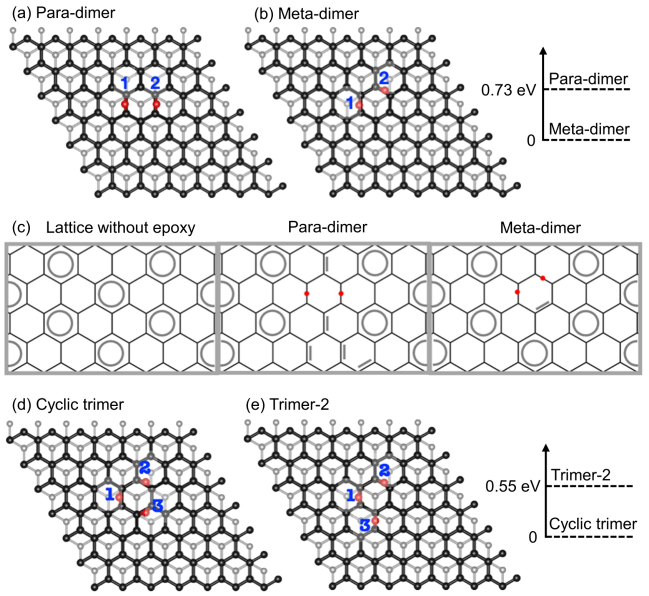

FIG. 1. Comparison of cluster isomers. (a) Para-dimer. (b) Meta-dimer. Relative energy for (a) and (b) is shown on the right. (c) The illustration of Clar's structure for the pristine lattice, para-dimer, and meta-dimer. (d) Cyclic trimer. (e) Trimer-2. The relative energy for (d) and (e) is shown on the right.

building from the metadimer and predicted the relative probability of the corresponding isomers by counting the number of π-sextets. For trimers, we considered the two most probable isomers. The first one is a cyclic trimer when the third epoxy is added within the same honeycomb as that of the dimer [Fig. 1(d)]. The second isomer is formed when the third epoxy is added outside the honeycomb at the nearest neighbor site (i.e., at a site separated by a single C—C bridge). We refer to this isomer as trimer-2 [Fig. 1(e)]. Based on Clar's structure, the cyclic trimer maximizes the number of π sextets (Fig. S2). Indeed, VdW-DFT calculation shows that the cluster energy for cyclic trimer is 0.55 eV lower than that of trimer-2.

As the cluster grows, the number of isomers increases significantly. To manage this, we restricted our search for the most probable isomer for a cluster with $k+1$ epoxies by fixing the starting point using the most stable cluster hosting k epoxies. For example, knowing that cyclic trimers are the most stable cluster made of three epoxies, we built tetramer isomers by placing one additional epoxy next to the cyclic trimer. Three most probable tetramer isomers were studied. In two of them, the fourth epoxy is placed at the nearest neighbor position (i.e., separated by a single C—C bridge from an epoxy in the cyclic trimer [tetramer-1 in Fig. 2(a) and tetramer-2 in Fig. 2(b)]. In the third isomer (tetramer-3), the fourth epoxy is separated by two C—C bridges [Fig. 2(c)]. Among these, tetramer-1 and 2 have eight π sextets, while tetramer-3 has only six π sextets (Fig. S3), making tetramer-1 and 2 more probable. VdW-DFT–based calculation of cluster energy agrees with this

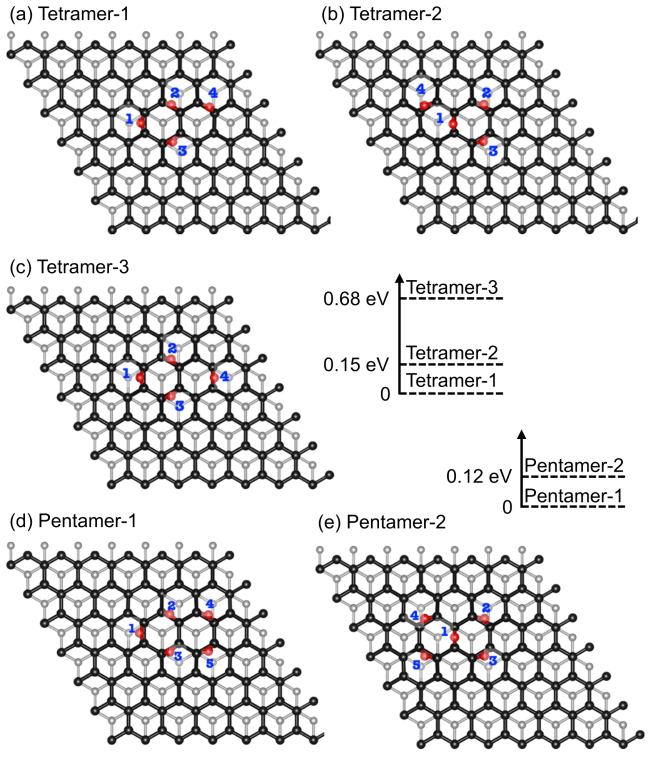

FIG. 2. Comparison of cluster isomers. (a) Tetramer-1. (b) Tetramer-2. (c) Tetramer-3. (d) Pentamer-1. (e) Pentamer-2.

prediction. Tetramer-1 and 2 have the lowest cluster energy with a small energy difference of 0.15 eV among them, while tetramer-3 has 0.68 eV higher energy than that of tetramer-1.

Given that both tetramer-1 and 2 have a similar energy, we built pentamer isomers by placing an additional epoxy in the meta configuration to the fourth epoxy of the two tetramer isomers [Figs. 2(d) and 2(e)]. The resulting two pentamer isomers have equal number of π sextets (seven) indicating that they may have a similar probability (Fig. S4). This is also confirmed by VdW-DFT calculations that indicate that the difference in energy between these two isomers is quite small (0.12 eV).

Based on the organization of epoxies in tetramer and pentamer isomers, we note a few interesting points. In tetramer-2, there are four epoxy pairs in the meta configuration [Fig. 2(b)]. In contrast, in tetramer-1, there are only three epoxy pairs in the meta configuration. The pair formed by the second and fourth epoxy of tetramer-1 is less favorable than the meta configuration [Fig. 2(a)]. Given that the epoxy pair in meta configuration is most stable, tetramer-2 could be favored over tetramer-1. Similarly, pentamer-2 hosts two cyclic trimers whereas pentamer-1 hosts only one cyclic trimer [Figs. 2(d) and 2(e)]. These observations indicate that tetramer-2 and its subsequent evolution into pentamer-2 could be favored over tetramer-1 and pentamer-1, respectively. However, the energy difference predicted by VdW-DFT between these two sets of isomers is too small to confirm this hypothesis. This motivated us to compare the energy of larger clusters.

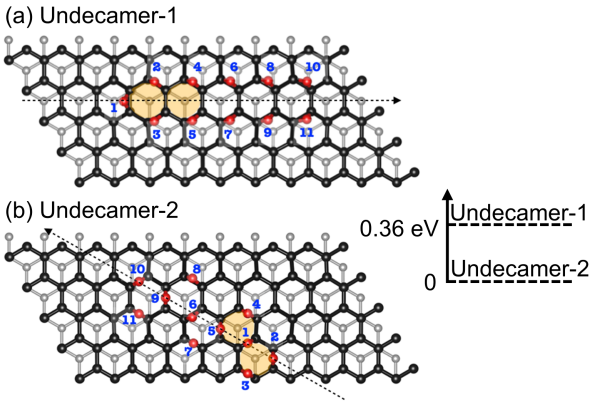

FIG. 3. (a) The structures of dimer chain (undecamer-1). (b) The structure of trimer chain (undecamer-2). The shaded honeycombs highlight the propagation of chains from pentamer. The arrows mark the direction of chain.

We note that a supercell made of 7×7 periodic unit cells is not large enough for the larger clusters to avoid interactions between the epoxy groups in the neighboring periodic replica. Given that the pentamer isomers start to take the shape of a linear chain, we performed calculations on an elongated supercell made of 5×10 periodic unit cells. This way, we made sure that epoxies in an image will not interact with other epoxies in the neighboring replicas (Fig. S5).

We built two undecamer isomers following the two distinct epoxy addition schemes used to build pentamer-1 and -2 starting from the cyclic trimer. Briefly, epoxy addition was always carried out at the nearest neighbor site. In the case of the linear chain extending from pentamer-2, the meta configuration was always ensured for additional epoxies. This led to a chain of cyclic trimer [undecamer-2, Fig. 3(b)]. In the other scheme, a chain of dimer was obtained [undecamer-1, Fig. 3(a)]. The number of π sextets in both cases were equal (Fig. S6); however, in this case, VdW-DFT calculations could confirm our prior assertion. The undecamer-2 reduces the cluster energy by 0.36 eV in comparison to undecamer-1, which makes the former more favorable. Therefore, the linear epoxy cluster on the graphitic lattice is expected to be composed of the chain of cyclic trimers.

By comparing the cyclic trimer chain (undecamer-2) with the dimer chain (undecamer-1), one observes an interesting structural registry of the chain propagation direction with the graphitic lattice. The latter always propagates along the zigzag direction of the lattice, whereas the former always propagates along the armchair direction (direction highlighted by arrows in Fig. 3). The unique chain propagation can be also easily visualized in the Clar's sextet diagram for the two undecamer isomers (Fig. S6). This registry of cyclic trimer chain exclusively along the armchair direction is because propagation along the zigzag

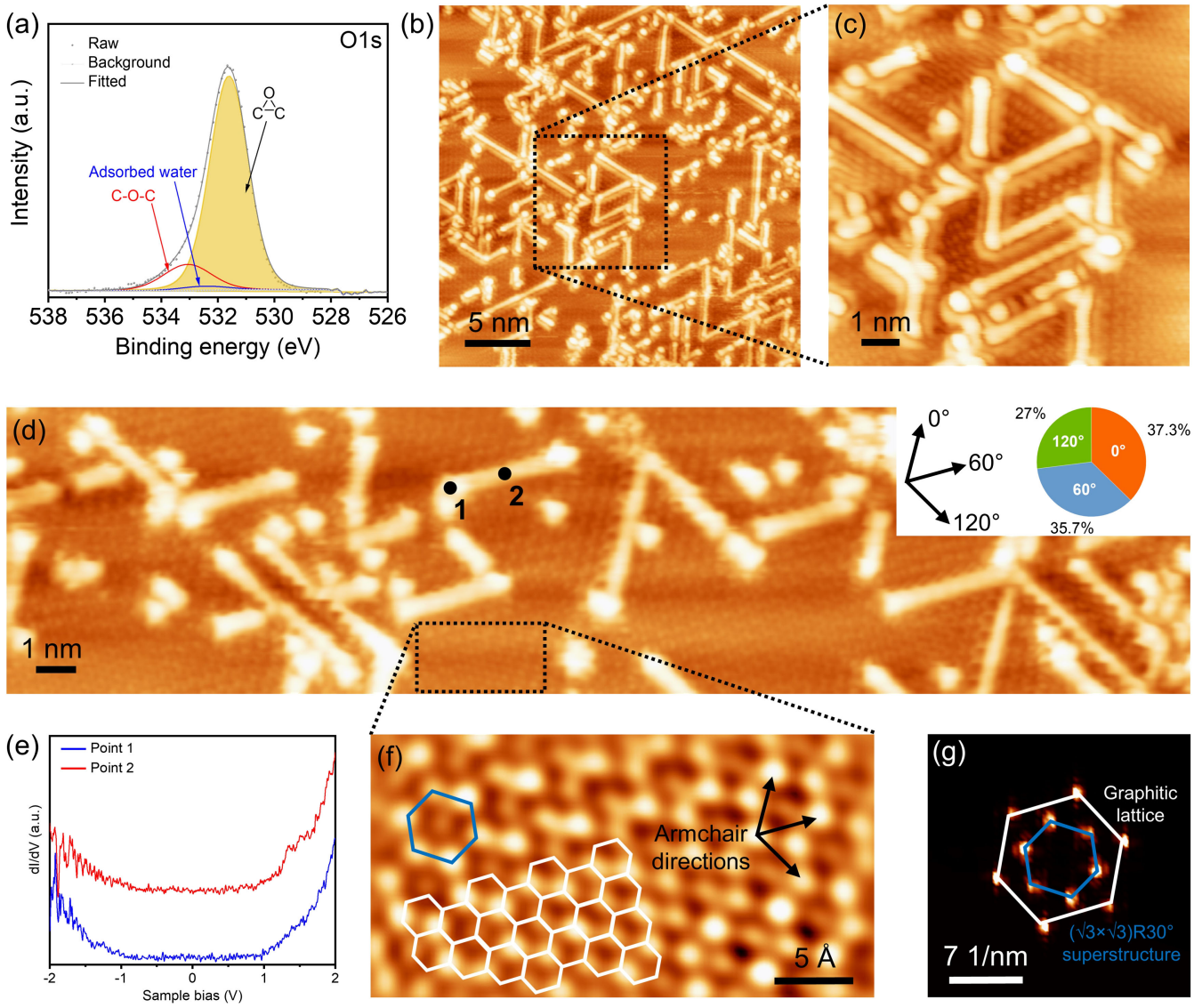

FIG. 4. Validation of the structure of epoxy chain. (a) The O1s XPS spectrum from mildly oxidized HOPG. The adsorbed water peak was determined by XPS experiment on HOPG that was not subjected to oxidation (Fig. S8). (b) LTSTM image of mildly oxidized HOPG. (c) A high-resolution LTSTM scan from an area enclosed by the black square in (b). (d) High-resolution LTSTM image from another area. The inset shows the orientation of the linear chain with distribution for orientation in a pie diagram. The orientations were obtained from 126 linear chains in panel (b). The bias voltage and tunneling current for STM images in (b)–(d) were +2 V and 0.5 nA, respectively. (e) STS spectra collected from points 1 and 2 in (d). (f) Magnified view of the pristine graphitic area from panel (d). The graphene lattice is superimposed on the image to illustrate the three armchair directions. The $(\sqrt{3} \times \sqrt{3})$R30° superstructure of graphite is illustrated by a blue hexagon. (g) A fast Fourier transform generated from an area in panel (f). Hexagons representing graphitic lattice and $(\sqrt{3} \times \sqrt{3})$R30° superstructure are superimposed on top of the fast Fourier transform.

direction would violate the maximum number of bonds for the C atom. In the armchair direction, two neighboring graphitic honeycombs share an epoxy at their shared edge [i.e., epoxy # 1, 5, 6, 9, and 10 in Fig. 3(b)], with five epoxies in two neighboring honeycombs.

As discussed before, a chain running along the zigzag direction (Fig. S7) with oxygen in para configuration is often discussed in the literature to explain the crack propagation in the graphene lattice [30,33]. Compared to a cyclic trimer chain with same number of oxygen, this configuration leads to a larger disruption in the aromaticity of the lattice, reflected in a lower number of π sextets (Fig. S7), and therefore, is less likely. VdW-DFT calculations confirm that the chain in the para configuration results in significantly higher system energy (1.02 eV) compared to the cyclic trimer chain.

Next, we oxidized a graphitic substrate and carried out LTSTM imaging to validate our prediction on the formation and organization of epoxies. For this, a mild oxidation of highly oriented pyrolytic graphite (HOPG) was carried out

by a short exposure to a flow of O_3. High-resolution x-ray photoelectron spectroscopy (XPS) revealed the onset of an O1s peak [531.6 eV, Fig. 4(a)], which could be assigned to the epoxy group [55]. For LTSTM imaging, the oxidized substrate was quickly transferred into the ultrahigh vacuum chamber of the instrument and the substrate was cooled down to 4 K to avoid contamination and arrest further cluster aggregation [56].

Scanning the epoxidized substrate with a bias voltage of +2 V, we observed several bright linear features [Fig. 4(b)]. Higher resolution scans revealed lattice-resolved graphite surface over which the linear features could be reproduced, confirming that these features were not artifacts but clusters [Fig. 4(c)]. The scanning tunneling spectroscopy (STS) spectra [Fig. 4(e)] obtained from these features [points 1 and 2 in Fig. 4(d)] revealed the presence of a band gap (1.7–1.9 eV), which is expected for the epoxy group, and is consistent with the reported band gap for graphene oxide (∼1.6 eV) [57]. In combination with the O1s XPS data, this confirms that these clusters are indeed composed of epoxies. Ether clusters can be ruled out because ether group has sp^2 hybridization and a large band gap is not expected [58].

The angles between the linear features were restricted to 0°, 60°, and 120°, indicating an underlying threefold symmetry [inset of Fig. 4(d), Figs. S9, S10]. This could arise from a structural registry between the linear features and the graphitic lattice. With high-resolution image and the corresponding fast Fourier transform [Figs. 4(f) and 4(g)], we could resolve the graphitic lattice including $(\sqrt{3}\times\sqrt{3})$R30° superstructure of graphite [59–65] and armchair and zigzag directions. This made it clear that the linear features propagated exclusively along the three armchair directions of the lattice. This validates that the linear features cannot be dimer chain, and are likely trimer chain.

Simulated STM images for cyclic epoxy trimer had a good agreement with the smallest features in the STM image (Fig. S11). The simulated STM images for trimer chain were also consistent with the STM image of the chains acquired at bias voltages of +2 V and −1.5 V (Fig. S12).

This study systematically reveals that the epoxy groups form linear clusters on the graphitic lattice to minimize the total energy of the system by minimizing the disruption of the aromaticity. Our theoretical predictions based on VdW-DFT calculation and Clar's aromatic π-sextet rule in combination with LTSTM imaging of the clusters confirm that not only do clusters organize in the shape of a linear chain, but they follow a unique structural pattern. They first form a cyclic epoxy trimer that then propagates as a chain of cyclic trimers along the armchair direction of the graphitic lattice.

Overall, we resolve the longstanding question on the structure of epoxy cluster on the graphitic lattice, a feature that has been central to the discussion on defects formation including crack formation in graphite, unzipping of carbon nanotubes, and the formation of vacancy defects in graphene. We reveal that the epoxy cluster propagates in the shape of a linear chain of cyclic epoxy trimers and that it has a unique structural registry with the graphitic lattice, i.e., it propagates exclusively along the armchair direction of the lattice. This understanding will allow one to develop highly precise techniques for defect incorporation, functionalization, and patterning of graphitic materials at the atomic scale with applications in electronics, optoelectronics, magnetism, and mass transport.

We acknowledge the host institution EPFL for support. Parts of the project were funded by the European Research Council Starting grant (805437-UltimateMembranes), and Swiss National Supercomputing Center, CSCS, (production projects s860 and s953). C. A. P. would like to acknowledge CSCS grant under project ID s1141 and thank PRACE for awarding access to the Fenix Infrastructure resources at CSCS, which are partially funded from the European Union's Horizon 2020 research and innovation programme through the ICEI project under grant agreement No. 800858. K. V. A., N. M., M. T. V., and S. L. conceived the project. M. T. V. carried out the DFT calculations. S. L. performed experiments and corresponding analyses. S. H. helped with the sample preparation. C. A. P. contributed to the simulated STM images. All authors discussed the results and wrote the manuscript.

*These authors contributed equally to this work.
†Corresponding author: nicola.marzari@epfl.ch
‡Corresponding author: kumar.agrawal@epfl.ch

[1] D. C. Marcano, D. V. Kosynkin, J. M. Berlin, A. Sinitskii, Z. Sun, A. Slesarev, L. B. Alemany, W. Lu, and J. M. Tour, Improved synthesis of graphene oxide, ACS Nano **4**, 4806 (2010).
[2] T. Nakajima and Y. Matsuo, Formation process and structure of graphite oxide, Carbon **32**, 469 (1994).
[3] W. Gao, L. B. Alemany, L. Ci, and P. M. Ajayan, New insights into the structure and reduction of graphite oxide, Nat. Chem. **1**, 403 (2009).
[4] D. V. Kosynkin, A. L. Higginbotham, A. Sinitskii, J. R. Lomeda, A. Dimiev, B. K. Price, and J. M. Tour, Longitudinal unzipping of carbon nanotubes to form graphene nanoribbons, Nature (London) **458**, 872 (2009).
[5] N. L. Rangel, J. C. Sotelo, and J. M. Seminario, Mechanism of carbon nanotubes unzipping into graphene ribbons, J. Chem. Phys. **131**, 031105 (2009).
[6] X. Wang and H. Dai, Etching and narrowing of graphene from the edges, Nat. Chem. **2**, 661 (2010).
[7] F. Cataldo, G. Compagnini, G. Patané, O. Ursini, G. Angelini, P. R. Ribic, G. Margaritondo, A. Cricenti, G. Palleschi, and F. Valentini, Graphene nanoribbons produced by the oxidative unzipping of single-wall carbon nanotubes, Carbon **48**, 2596 (2010).

[8] S. P. Koenig, L. Wang, J. Pellegrino, and J. S. Bunch, Selective molecular sieving through porous graphene, Nat. Nanotechnol. **7**, 728 (2012).
[9] S. Huang, S. Li, L. F. Villalobos, M. Dakhchoune, M. Micari, D. J. Babu, M. T. Vahdat, M. Mensi, E. Oveisi, and K. V. Agrawal, Millisecond lattice gasification for high-density CO2- and O2-sieving nanopores in single-layer graphene, Sci. Adv. **7**, eabf0116 (2021).
[10] S. P. Surwade, S. N. Smirnov, I. V. Vlassiouk, R. R. Unocic, G. M. Veith, S. Dai, and S. M. Mahurin, Water desalination using nanoporous single-layer graphene, Nat. Nanotechnol. **10**, 459 (2015).
[11] C. Mattevi, G. Eda, S. Agnoli, S. Miller, K. A. Mkhoyan, O. Celik, D. Mastrogiovanni, G. Granozzi, E. Carfunkel, and M. Chhowalla, Evolution of electrical, chemical, and structural properties of transparent and conducting chemically derived graphene thin films, Adv. Funct. Mater. **19**, 2577 (2009).
[12] G. Eda and M. Chhowalla, Chemically derived graphene oxide: Towards large-area thin-film electronics and optoelectronics, Adv. Mater. **22**, 2392 (2010).
[13] D. Jariwala, V. K. Sangwan, L. J. Lauhon, T. J. Marks, and M. C. Hersam, Carbon nanomaterials for electronics, optoelectronics, photovoltaics, and sensing, Chem. Soc. Rev. **42**, 2824 (2013).
[14] Z. Mutlu, P. H. Jacobse, R. D. McCurdy, J. P. Llinas, Y. Lin, G. C. Veber, F. R. Fischer, M. F. Crommie, and J. Bokor, Bottom-up synthesized nanoporous graphene transistors, Adv. Funct. Mater. **31**, 2103798 (2021).
[15] T. Gokus, R. R. Nair, A. Bonetti, M. Böhmler, A. Lombardo, K. S. Novoselov, A. K. Geim, A. C. Ferrari, and A. Hartschuh, Making graphene luminescent by oxygen plasma treatment, ACS Nano **3**, 3963 (2009).
[16] F. Bonaccorso, Z. Sun, T. Hasan, and A. C. Ferrari, Graphene photonics and optoelectronics, Nat. Photonics **4**, 611 (2010).
[17] K. P. Loh, Q. Bao, G. Eda, and M. Chhowalla, Graphene oxide as a chemically tunable platform for optical applications, Nat. Chem. **2**, 1015 (2010).
[18] O. V. Yazyev and L. Helm, Defect-induced magnetism in graphene, Phys. Rev. B **75**, 125408 (2007).
[19] K. Celebi, J. Buchheim, R. M. Wyss, A. Droudian, P. Gasser, I. Shorubalko, J. Il Kye, C. Lee, and H. G. Park, Ultimate permeation across atomically thin porous graphene, Science **344**, 289 (2014).
[20] L. F. Villalobos *et al.*, Bottom-up synthesis of graphene films hosting atom-thick molecular-sieving apertures, Proc. Natl. Acad. Sci. U.S.A. **118**, e2022201118 (2021).
[21] Z. Yuan, G. He, S. Faucher, M. Kuehne, S. X. Li, D. Blankschtein, and M. S. Strano, Direct chemical vapor deposition synthesis of porous single-layer graphene membranes with high gas permeances and selectivities, Adv. Mater. **33**, 2104308 (2021).
[22] C. Cheng, S. A. Iyengar, and R. Karnik, Molecular size-dependent subcontinuum solvent permeation and ultrafast nanofiltration across nanoporous graphene membranes, Nat. Nanotechnol. **16**, 989 (2021).
[23] Y. Yang, X. Yang, L. Liang, Y. Gao, H. Cheng, X. Li, M. Zou, R. Ma, Q. Yuan, and X. Duan, Large-area graphene-nanomesh/carbon-nanotube hybrid membranes for ionic and molecular nanofiltration, Science **364**, 1057 (2019).
[24] D. Pandey, R. Reifenberger, and R. Piner, Scanning probe microscopy study of exfoliated oxidized graphene sheets, Surf. Sci. **602**, 1607 (2008).
[25] K. N. Kudin, B. Ozbas, H. C. Schniepp, R. K. Prud'homme, I. A. Aksay, and R. Car, Raman spectra of graphite oxide and functionalized graphene sheets, Nano Lett. **8**, 36 (2008).
[26] S. Park and R. S. Ruoff, Chemical methods for the production of graphenes, Nat. Nanotechnol. **4**, 217 (2009).
[27] K. A. Mkhoyan, A. W. Contryman, J. Silcox, D. A. Stewart, G. Eda, C. Mattevi, S. Miller, and M. Chhowalla, Atomic and electronic structure of graphene-oxide, Nano Lett. **9**, 1058 (2009).
[28] M. Z. Hossain *et al.*, Chemically homogeneous and thermally reversible oxidation of epitaxial graphene, Nat. Chem. **4**, 305 (2012).
[29] C. Gómez-Navarro, R. T. Weitz, A. M. Bittner, M. Scolari, A. Mews, M. Burghard, and K. Kern, Electronic transport properties of individual chemically reduced graphene oxide sheets, Nano Lett. **7**, 3499 (2007).
[30] G. Lee, B. Lee, J. Kim, and K. Cho, Ozone adsorption on graphene: *Ab initio* study and experimental validation, J. Phys. Chem. C **113**, 14225 (2009).
[31] M. T. Nguyen, R. Erni, and D. Passerone, Two-dimensional nucleation and growth mechanism explaining graphene oxide structures, Phys. Rev. B **86**, 115406 (2012).
[32] J. L. Li, K. N. Kudin, M. J. McAllister, R. K. Prud'homme, I. A. Aksay, and R. Car, Oxygen-driven unzipping of graphitic materials, Phys. Rev. Lett. **96**, 176101 (2006).
[33] T. Sun and S. Fabris, Mechanisms for oxidative unzipping and cutting of graphene, Nano Lett. **12**, 17 (2012).
[34] A. Bagri, C. Mattevi, M. Acik, Y. J. Chabal, M. Chhowalla, and V. B. Shenoy, Structural evolution during the reduction of chemically derived graphene oxide, Nat. Chem. **2**, 581 (2010).
[35] R. Larciprete, S. Fabris, T. Sun, P. Lacovig, A. Baraldi, and S. Lizzit, Dual path mechanism in the thermal reduction of graphene oxide, J. Am. Chem. Soc. **133**, 17315 (2011).
[36] See Supplemental Material at http://link.aps.org/supplemental/10.1103/PhysRevLett.131.168001 for experimental methods, supplemental notes, and supplemental figures, which includes Refs. [37–51].
[37] P. Giannozzi *et al.*, QUANTUM ESPRESSO: A modular and open-source software project for quantum simulations of materials, J. Phys. Condens. Matter **21**, 395502 (2009).
[38] P. Giannozzi *et al.*, Advanced capabilities for materials modelling with QUANTUM ESPRESSO, J. Phys. Condens. Matter **29**, 465901 (2017).
[39] K. Lejaeghere *et al.*, Reproducibility in density functional theory calculations of solids, Science **351**, aad3000 (2016).
[40] G. Prandini, A. Marrazzo, I. E. Castelli, N. Mounet, and N. Marzari, Precision and efficiency in solid-state pseudopotential calculations, npj Comput. Mater. **4**, 72 (2018).
[41] K. Lee, É. D. Murray, L. Kong, B. I. Lundqvist, and D. C. Langreth, Higher-accuracy van Der Waals density functional, Phys. Rev. B **82**, 081101 (2010).
[42] A. V. Yakutovich *et al.*, AiiDAlab—an ecosystem for developing, executing, and sharing scientific workflows, Comput. Mater. Sci. **188**, 110165 (2021).

[43] J. Hutter, M. Iannuzzi, F. Schiffmann, and J. Vandevondele, Cp2k: Atomistic simulations of condensed matter systems, Comput. Mol. Sci. **4**, 15 (2014).
[44] G. Pizzi, A. Cepellotti, R. Sabatini, N. Marzari, and B. Kozinsky, AiiDA: Automated interactive infrastructure and database for computational science, Comput. Mater. Sci. **111**, 218 (2016).
[45] J. VandeVondele and J. Hutter, Gaussian basis sets for accurate calculations on molecular systems in gas and condensed phases, J. Chem. Phys. **127**, 114105 (2007).
[46] S. Goedecker and M. Teter, Separable dual-space gaussian pseudopotentials, Phys. Rev. B **54**, 1703 (1996).
[47] J. P. Perdew, K. Burke, and M. Ernzerhof, Generalized gradient approximation made simple, Phys. Rev. Lett. **77**, 3865 (1996).
[48] S. Grimme, J. Antony, S. Ehrlich, and H. Krieg, A consistent and accurate *ab initio* parametrization of density functional dispersion correction (DFT-D) for the 94 elements H-Pu, J. Chem. Phys. **132**, 154104 (2010).
[49] I. Horcas, R. Fernández, J. M. Gómez-Rodríguez, J. Colchero, J. Gómez-Herrero, and A. M. Baro, WSXM: A software for scanning probe microscopy and a tool for nanotechnology, Rev. Sci. Instrum. **78**, 013705 (2007).
[50] E. Clar, *The aromatic Sextet* (JohnWiley & Sons, Ltd, London and New York, 1972).
[51] E. Clar, *Polycyclic Hydrocarbons* (Academic Press, New York, 1964).
[52] M. Baldoni, A. Sgamellotti, and F. Mercuri, Electronic properties and stability of graphene nanoribbons: An interpretation based on clar sextet theory, Chem. Phys. Lett. **464**, 202 (2008).
[53] D. Wu, X. Gao, Z. Zhou, and Z. Chen, *Graphene Chemistry: Theoretical Perspectives*, edited by D.-E. Jiang and Z. Chen (John Wiley & Sons, Ltd., 2013), 10.1002/9781118691281.
[54] T. Wassmann, A. P. Seitsonen, A. M. Saitta, M. Lazzeri, and F. Mauri, Clar's theory, π-electron distribution, and geometry of graphene nanoribbons, J. Am. Chem. Soc. **132**, 3440 (2010).
[55] R. Larciprete, P. Lacovig, S. Gardonio, A. Baraldi, and S. Lizzit, Atomic oxygen on graphite: Chemical characterization and thermal reduction, J. Phys. Chem. C **116**, 9900 (2012).
[56] P. V. Kumar, N. M. Bardhan, S. Tongay, J. Wu, A. M. Belcher, and J. C. Grossman, Scalable enhancement of graphene oxide properties by thermally driven phase transformation, Nat. Chem. **6**, 151 (2014).
[57] S. Katano, T. Wei, T. Sasajima, R. Kasama, and Y. Uehara, Localized electronic structures of graphene oxide studied using scanning tunneling microscopy and spectroscopy, Phys. Chem. Chem. Phys. **20**, 17977 (2018).
[58] B. R. Goldsmith, J. G. Coroneus, V. R. Khulap, A. A. Kane, G. A. Weiss, and P. G. Collins, Conductance-controlled point, Science **315**, 77 (2007).
[59] J. P. Rabe, M. Sano, D. Batchelder, and A. A. Kalatchev, Polymers on graphite and gold: Molecular images and substrate defects, J. Microsc. **152**, 573 (1988).
[60] H. A. Mizes and J. S. Foster, Long-range electronic perturbations caused by defects using scanning tunneling microscopy, Science **244**, 559 (1989).
[61] P. L. Giunta and S. P. Kelty, Direct observation of graphite layer edge states by scanning tunneling microscopy, J. Chem. Phys. **114**, 1807 (2001).
[62] Y. Kobayashi, K. I. Fukui, T. Enoki, K. Kusakabe, and Y. Kaburagi, Observation of zigzag and armchair edges of graphite using scanning tunneling microscopy and spectroscopy, Phys. Rev. B **71**, 193406 (2005).
[63] Y. Niimi, T. Matsui, H. Kambara, K. Tagami, M. Tsukada, and H. Fukuyama, Scanning tunneling microscopy and spectroscopy of the electronic local density of states of graphite surfaces near monoatomic step edges, Phys. Rev. B **73**, 085421 (2006).
[64] Y. Kobayashi, K. I. Fukui, T. Enoki, and K. Kusakabe, Edge state on hydrogen-terminated graphite edges investigated by scanning tunneling microscopy, Phys. Rev. B **73**, 125415 (2006).
[65] J. C. M. López, M. C. G. Passeggi, and J. Ferrón, Surface superstructures in highly oriented pyrolytic graphite surfaces after Ar^+ Bombardment, Surf. Sci. **602**, 671 (2008).